Fault Diagnosis of Rolling Bearing Based on Variational Mode Decomposition and Improved Canberra Distance in Symmetrized Dot Pattern Image

Wei Wang, Jian Wang, Yongjian Sun*

*School of Electrical Engineering, University of Jinan, Jinan, Shandong, China

Corresponding author: Yongjian Sun, Electrical Engineering, University of Jinan, Jinan, Shandong, China. Email: sunyongjian2006@163.com

A B S T R A C T

The classification of time series is an important work in mechanical fault diagnosis. In recent years, image-based signal processing methods have been widely used in bearing fault diagnosis. However, there are still some problems in the signal classification of multiple fault types and weak fault characteristics. In order to improve the classification accuracy of time series, a diagnosis method based on variable mode decomposition (VMD) and improved Canberra distance is proposed. In this method, the decomposed signal is first converted into a symmetrized dot pattern. Then the image features are extracted using Canberra distance and maximum eigenvalue. Through the obtained features, the accurate diagnosis of bearing vibration signal is realized. The experimental results show that the improved Canberra distance has high classification accuracy.

Keywords: Rolling bearing, Symmetrized Dot Pattern, Variational mode decomposition, Canberra distance, Fault diagnosis

Introduction

Rolling bearing is essential for reducing the friction coefficient between the shaft and the shell. In many industries, such as large chemical industries, integration of electromechanical, aerospace, improving the reliability and safety of the bearing is also the guarantee of the stable operation of equipment and personal safety. The failure of the rolling bearing has not fully reached the design life [1]. If the rolling bearings fail, it is likely to cause the entire equipment to stop operation and stagnate industrial production, resulting in unavoidable losses [2]. Therefore, the fault diagnosis of rolling bearing is a very important research field [3].

1. The main structure of rolling bearing consists of four parts:
2. The inner ring is a bearing ring, and the outer surface of its raceway.
3. The outer ring which is fixed on the shell or seat supports the rolling body.
4. The sliding coefficient of the outer ring and the inner ring is reduced, and the sliding friction is converted to the problem of the rolling friction.

A cage that divides the rolling elements evenly and makes the rolling elements rotate stably [4].

The problem of this paper is the fault diagnosis of rolling bearing. Fault diagnosis is a meaningful and difficult problem in mechanical equipment. The difficulty of this problem is to use the vibration signal to determine whether the bearing is faulty. Fault diagnosis is realized by analyzing the vibration signal. It is an effective method to improve the signal analysis technology. In addition, it is also a good method to improve the image feature extraction technology. The spectrum analyzer first uses the spectrum of the original signal of the rolling bearings to analyze the fault of the bearings [5]. Spectrum analysis cannot solve the effect of noise on the diagnosis of fault. With the continuous improvement of industrial production requirements and the rapid development of network technology, various new intelligent rolling bearings diagnostic methods have appeared in information science and network technology [6,7]. In particular, many computer technologies such as neural network computing and application, deep learning and other computer technologies have been used in the diagnosis of rolling bearings [8,9]. With the development of artificial intelligence, the new technologies

of rolling bearing fault diagnosis have emerged endlessly [10]. For example, the application of element learning to the diagnosis of bearing faults and the application of multitask convolutional neural networks to diagnosis and localization [11]. There is also a new type of bearing failure to quickly diagnose measuring instruments through the improvement of the source of information collection [12]. Pre-processing the original collected rolling bearing vibration signal. Due to the signal collection process, the collected signal contains noise signals. In order to better distinguish the signal, the signal needs to be processed with noise reduction and retains the effective information of the fault [13].

Signal processing is a direct processing of the original noise signal, where the discrete time signal has multiple signal processing methods, such as digital filter [14]. There are also various signal decomposition methods to choose the best filtering band, such as variational mode decomposition, wavelet packet decomposition, enhanced periodic mode decomposition and adaptive periodic mode decomposition [15,16]. This method decomposes the signal into different information of various frequency bands, which can reduce the noise of covering the fault information [17]. Using different signal decomposition methods, the number of decomposition layers is usually different, and the fault information and functional information contained in each layer are different. There are different processing methods after signal extraction, such as using complex wavelet data packet energy entropy to process the processing signal [18]. There is also a Bayesian optimization method using a Bayesian neural network to deal with the noise signal of the rolling bearing [19,20]. This method can be used to process the data of rolling bearings. In summary, the goal of data processing is to eliminate the influence of noise on fault feature extraction. And the filtering method has been applied to the fault diagnosis of rolling bearings. For example, the automatic filtering scheme has been used in rolling bearing fault diagnosis [21].

Rolling bearing signals can also be converted to various other forms of data, such as time domain diagrams and frequency domain charts. These images can analyze the vibration signals from different angles [22]. The development of image computing and analysis technology is very good to combine bearing vibration signals with digital images. Vibration data can be converted into different images to analyze the original discrete signal. For example, the signal is transformed into the SDP image. Then the convolution neural network is used to identify the SDP features under different vibration states [23,24]. The fault diagnosis method based on image has been applied to rolling bearing.

The research object of this paper is rolling bearing. This paper adopts the image processing method of data conversion. The feature extraction of different types of bearing fault information is realized through images. Our goal is to achieve accurate classification of bearing faults by converting data into SDP and extracting image features of SDP. And our research objective is to achieve more than 98% accuracy in bearing fault diagnosis. In order to monitor the status of rolling bearings and prevent accidents, our research team has carried out feature extraction, feature reconstruction, feature calculation and feature recognition for bearing fault information. We classify faults by extracting image features of different faults. We extracted, analyzed and set the range of different fault characteristics. When the fault

characteristics are within the range, we can determine the fault type. Through extensive experimental data analysis, useful information can be extracted from fault information through convolution neural network [25]. The characteristics of rolling bearing faults can also be diagnosed by pseudo fourth-order moment [26]. SDP images can also be used to diagnose rolling bearing faults under four working conditions through improved Chebyshev distance and improved Manhattan distance [27, 28]. Based on the aforementioned research results, this paper redesigns the signal decomposition scheme and improves the Canberra distance. A fault diagnosis method for bearings based on variational mode decomposition (VMD) and Canberra distance is proposed.

The remainder of this paper is organized as follows: VMD decomposition and image processing methods are introduced in section 2, and a formula for improving the Canberra distance is given. The experimental design and simulation are carried out in section 3. The accuracy of Canberra distance and improved Canberra distance is compared in section 4. Comparing the accuracy of different signal decomposition methods verifies the effectiveness of the diagnostic methods based on VMD and Canberra distance. Finally, conclusion remarks are given in section 5.

Basic principles

Variational mode decomposition

Variational mode decomposition can adaptively decompose the original signal, which can be transformed into the corresponding variational problem construction and solution. It is mainly divided into the following three steps.

The first step is to convert the real signal into an analytical signal. This step makes the signal have amplitude and phase in the complex domain. Hilbert transform to find the analytical signal, by multiplying with $e^{-j\omega_k t}$, the formula is as follows:

$$\left(\gamma(t) + \frac{j}{\pi t}\right) * v_k(t) \qquad (1)$$

The second step is to use $e^{-j\omega_k t}$ to correct the signal. By multiplying with the operator $e^{-j\omega_k t}$, the central band of $v_k(t)$ is modulated to the corresponding baseband, as shown in eq.2. The third step is to estimate the bandwidth of the signal. Calculate the square norm of the demodulation gradient, as shown in eq.3. The main purpose of this step is to ensure that the decomposed signal has its own center frequency. The constraint condition is that the sum of all modes is equal to the original signal.

$$\left[\left(\gamma(t) + \frac{j}{\pi t}\right) * v_k(t)\right] e^{-j\omega_k t} \qquad (2)$$

$$\min_{\{v_k\}\{w_k\}} \left\{ \sum_k \| \, | \, \partial_t [(\gamma(t) + \frac{j}{\pi t}) * v_k(t)] e^{-j\omega_k t} \|^2 \right\} \qquad (3)$$
$$\text{s.t. } \sum_k v_k = s$$

where, the v_k represents each mode after decomposition.

The above equation-constrained optimization problem is equivalent to an unconstrained optimization problem through the augmented Lagrang function, and finally each group of modal components v_k is obtained. The modal component calculation formula is shown in eq.4, and the center frequency calculation formula is shown in eq.5.

$$v_k^{n+1} = \frac{f(w) - \sum_{i \neq k} v_i(\omega) + \frac{\lambda(\omega)}{2}}{1 + 2\alpha(\omega_{ik} - \omega_k)^2} \qquad (4)$$

$$\omega_k^{n+1} = \frac{\int_0^\infty \omega |v_k^{n+1}(\omega)|^2 d\omega}{\int_0^\infty |v_k^{n+1}(\omega)|^2 d\omega} \qquad (5)$$

Symmetrized dot pattern

Vibration signal is a discrete signal that fluctuates within a certain amplitude range. The signal will become multiple signal components after the Variable mode decomposition in section 2.1. The next work to be done is to select a suitable signal component. Then convert this component into a Symmetrized dot pattern. Through the calculation of the amplitude of one-dimensional signal by eq.6, eq.7 and eq.8, the signal data are projected onto the polar coordinate space $Z(r(i), \Theta(i), \varphi(i))$ and converted into a more intuitive two-dimensional image. The information of the signal is amplified, and the feature information is more easily extracted. An amplitude signal of one-dimensional original data can be mapped to two symmetrical points in the two-dimensional SDP diagram. Then, by rotating different angles, multiple amplitude data can obtain multi-branch images like snowflakes in different angles.

$$r(n) = \frac{x_n - x_{min}}{x_{max} - x_{min}} \qquad (6)$$

$$\alpha(n) = \theta + \frac{x_{n+l} - x_{min}}{x_{max} - x_{min}} M \qquad (7)$$

$$\beta(n) = \theta - \frac{x_{n+l} - x_{min}}{x_{max} - x_{min}} M \qquad (8)$$

where, x_{max} and x_{min} represent respectively the minimum and maximum values of the original sample signal, the Θ is the angle of rotation between each branch, the l is to select the time interval parameters of the original signal, the M is the magnification of the angle, the x_n represents the nth amplitude of the signal.

Through the above formula, the time-varying signal in time domain can be converted into a binary image in polar coordinates. The principle of the transformation is shown in fig.1, which shows that SDP is rotationally symmetrical relative to the initial line.
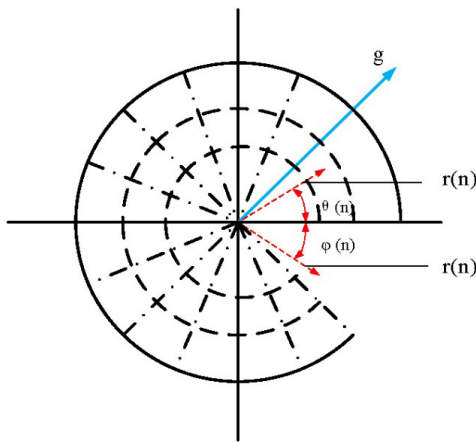

Figure 1: Symmetrized dot pattern.

Image processing

Image binarization is often used in image processing. Compared with color image and gray image, the binary image contains only black and white information, which reflects the contour of the image more clearly, and reduces the amount of information of the image, thereby improving the efficiency of the calculation. By converting the original image to gray image, each pixel is represented by gray information from 0 to 255, and by selecting the appropriate threshold, each pixel is converted to 0 or 255, so that the image has an obvious black and white effect. The binary conversion is shown in eq.9. Through conversion, the pixel information of such an image only needs to be represented by 0 and 255, highlighting the more important information such as shape and density of the image.

$$B(i,j) = \begin{cases} 255 & b(i,j) \geq T \\ 0 & b(i,j) < T \end{cases} \qquad (9)$$

Where, T is the threshold.

Canberra distance and its improvement

Canberra distance is very sensitive to changes in values greater than or equal to 0, and does not consider the correlation between variables. The calculation formula of Canberra distance between vector x_i and vector y_i is as follows eq.10.

$$d(x,y) = \sum_{i=1}^n \left| \frac{x_i - y_i}{|x_i| + |y_i|} \right| \qquad (10)$$

where, x_i and y_i represent respectively vectors of the same length.

In fig.2, the yellow line is the Euclidean distance from point O to point C, which is also the straight-line distance from (0,0) to (3,4). The value of this distance is 5. The green line is the Manhattan distance from point O to point C. It can only be calculated by adding up the lines in a parallel coordinate system. The relative distance between the horizontal coordinate point O and point C is 3, and the relative distance between the vertical coordinate point O and point C is 4. Therefore, the Manhattan distance is the sum of the horizontal and vertical distances. The distance from Manhattan is 7. Canberra distance is weighted based on Manhattan distance. The Manhattan distance from (0, 0) to (3, 4) is shown by the red line in the figure. Manhattan distance is 2.
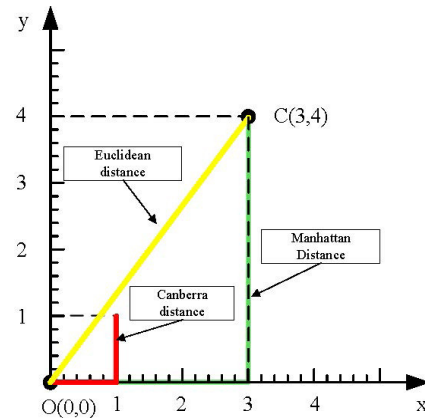

Figure 2: Schematic diagram of the three distances

The binary image can be regarded as a square matrix. Eigenvalue is a very important property of a matrix. Among many eigenvalues of a square matrix, the largest eigenvalue can best reflect the characteristics of the matrix. Therefore, we use eigenvalues to improve the Canberra distance. The eigenvalue calculation of matrix is shown in eq.11. Among the n eigenvalues, we select the largest eigenvalue as the feature of the image. As shown in eq.12. In the n Canberra distances of the image, we select the maximum value as the feature of the image. As shown in eq.12. Finally, we combine the maximum eigenvalue and the

maximum Canberra distance to obtain an improved Canberra distance as shown in eq.14.

$$|\lambda_n I - A(x, y)| = 0 \qquad (11)$$

where, A is the image matrix. I is the n-order identity matrix. n is the order.

$$\lambda_{max} = \max(\lambda_n) \qquad (12)$$

where, a is the maximum eigenvalue.

$$d_m = \frac{\sum_{i=1}^{n} d(x_i - y_i)}{n} \qquad (13)$$

where, d_m is the maximum Canberra distance.

$$D = \alpha * \lambda_{max} + \beta * d_m \qquad (14)$$

where, a and b are weighting coefficients.

Scheme Design

Scheme plan

The flow design of rolling bearing fault information is shown in fig.3. First, determine the number of layers of the VMD decomposition, and the sample data with different fault signal length of 6000 is selected. The appropriate decomposition level is determined by comparing the average instantaneous frequency of the signal. Then the moving average filter is used to filter the decomposed and reconstructed signals. Select different sequence length for filtering. By judging the correlation coefficient of signals before and after filtering, the optimal filtering sequence length is selected.
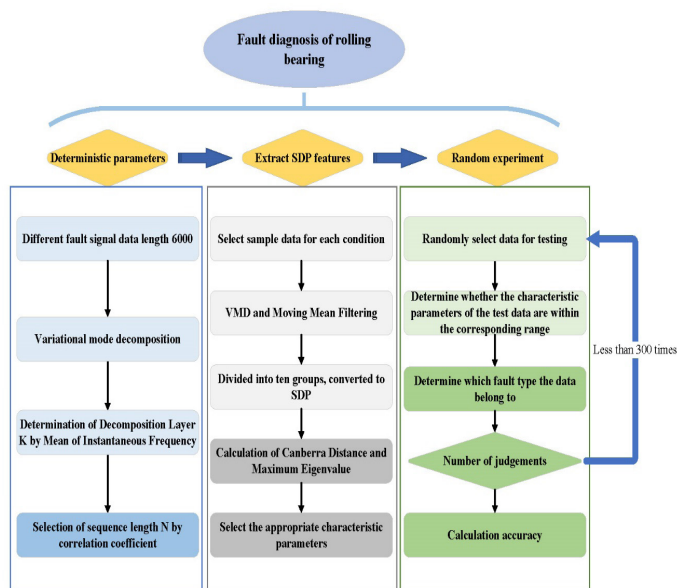

Figure 3: Process design

Use the SDP image to extract the features of different faults, and select the sample data under different working conditions. The data length is 6000, the VMD decomposition layer is K, and the moving average filter sequence length is N. Then the SDP images are plotted and the mean image is calculated. The Canberra distance and the largest eigenvalue between the mean image and the ten images are calculated. The optimal weight of Canberra distance and the largest eigenvalue is selected as the basis for fault diagnosis. Finally, randomly select data for testing. Determine which fault type the data belongs to by improving whether the Canberra distance is within the corresponding range, and calculate the accuracy.

4

Simulation experiment and analysis

This experiment is based on the data of Case Western Reserve University. There is a two-horsepower motor on the left and a power meter on the right. The fault diameters of 0.1778 mm and 0.3556 mm are selected for different types of faults. The bearing test platform is shown in fig.4.
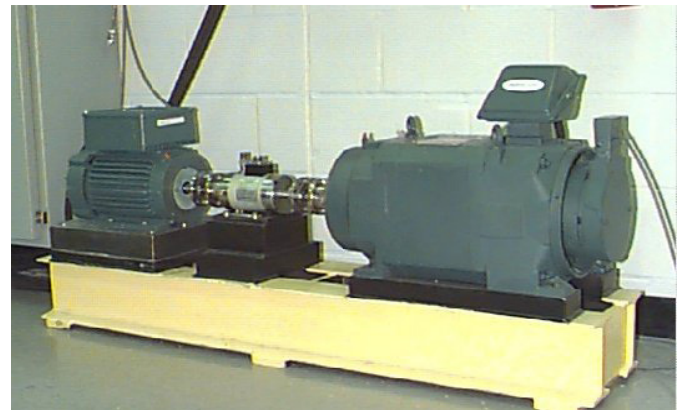

Figure 4: Rolling bearing Test Platform

In this paper, seven different bearing working conditions are selected. And the driving end frequency of the rolling bearing is 12khz. The seven working conditions are one normal working condition, two ball bearing faults, two inner ring faults and two outer ring faults. The collected bearing specifications and processing steps for each working condition are shown in fig.5, and the final unified test.
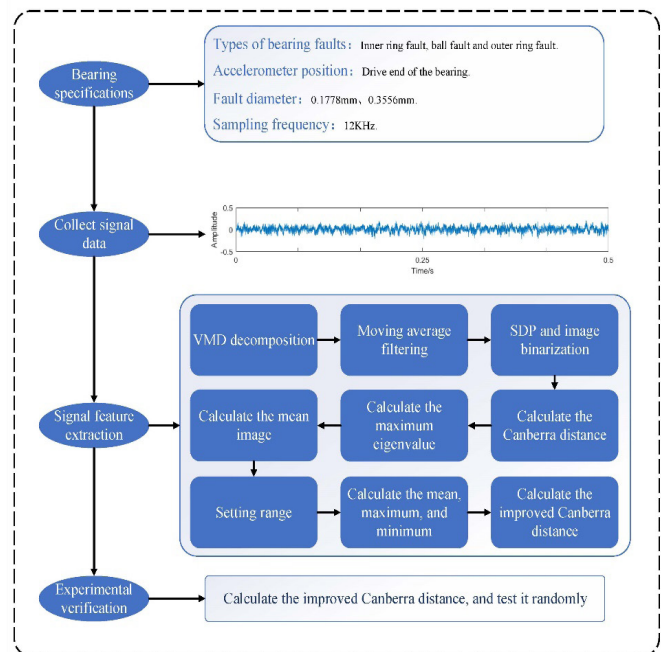

Figure 5: Flow chart of data processing

After each data collection, the obtained data is decomposed by VMD and filtered through a moving mean filter. Then, the processed data is divided into ten groups. According to the conversion formula of SDP, they are converted into two-dimensional images. Then the Canberra distance between the ten groups of images and the calculated mean image is calculated, and the improved Canberra Distance is obtained by weighting with the maximum eigenvalue. Then the corresponding improved Canberra Distance range for this group of data is calculated. Finally, the seven working conditions are tested randomly through this set range.

Different fault signals will produce different periodic fluctuations with time. Theoretically, the longer the data length selected, the more accurate the extraction of fault signal features. However, since the overall sample size is 120,000, if too much data is selected, the remaining test data will not be convincing. Therefore, the total data is divided into two sections. The first 60,000 data are used to extract features, and the last 60,000 are used for testing. The amount of data selected each time is 6000.

First of all, select a sample with 6,000 data length under normal working conditions. The diameter of the fault is 0.1778mm, and then the sample data is decomposed for VMD. When there are too many decomposition layers, the vibration signal will be over decomposed. Take the normal working condition as an example, when the signal is decomposed into four layers, the signal will be over decomposed. The signal components of the four-layer decomposition are shown in fig.6. The horizontal axis of the image is frequency. The vertical axis of the image is the amplitude of the signal component. It can be seen from the figure. As can be seen from fig.6, the center frequency of the first signal is almost the same as that of the third signal. This indicates that the signal is over-decomposed at frequency. Through experimental analysis, when the signal is decomposed into two layers, the signal decomposition effect is the best.
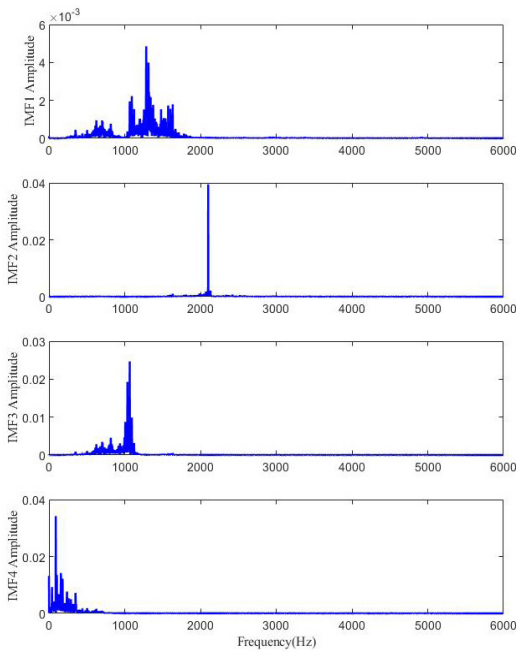

Figure 6: Spectrum diagram of four-layer component under normal working condition.

The decomposed signals obtained for each working condition are shown in fig.7, fig.8, fig.9 and fig.10. From the figures, we can see that the decomposed IMF2 contains less information, while IMF1 contains more signal characteristics of the original signal compared to IMF2. The IMF2 components of ball fault, inner ring fault and outer ring fault are all close to a straight line. Therefore, IMF1 is selected here as the characteristic signal for the subsequent analysis.

Convert the two groups of data decomposed under each working condition into SDP, as shown in fig.11-17 below. It can be seen that IMF2 under different working conditions is basically the same, which can be considered as the decomposition of noise signal. Therefore, IMF1 is used as a useful signal for feature extraction of subsequent processing.
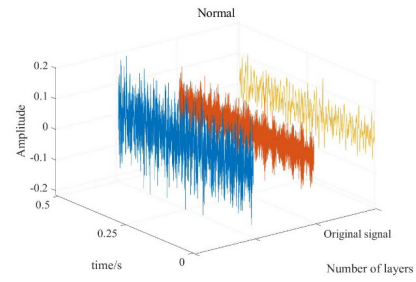

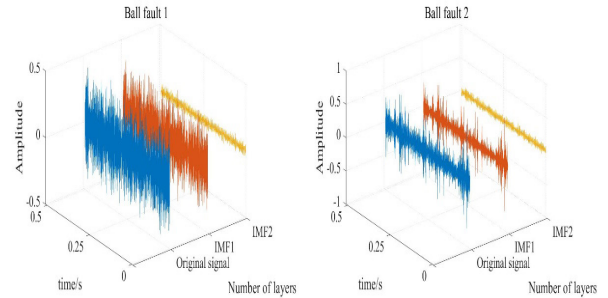**Figure 7:** Decomposition signal of normal working condition.
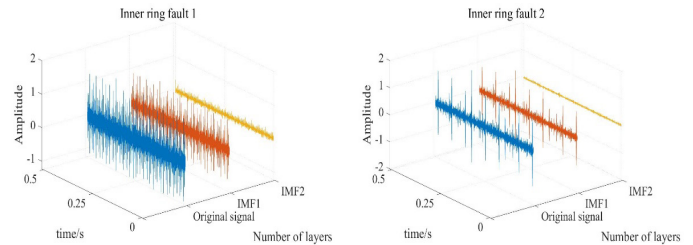

Figure 8: Decomposition signal of ball fault.

Figure 9: Decomposition signal of inner ring fault.
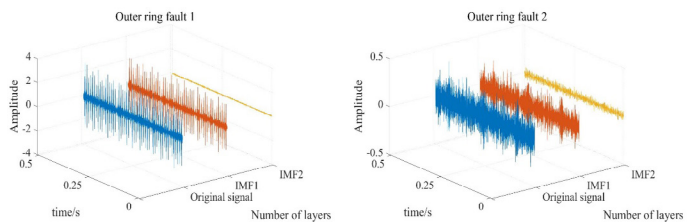
Figure 10: Decomposition signal of outer ring fault.

Figure 11: Component signal and mean image of normal working condition.

After the signal is decomposed by VMD, the data is divided into ten parts, and the data volume of each part is 600. Each data is converted into a symmetrical point pattern image according to the SDP conversion formula, as shown in fig.18. It can be seen from the figure that the SDP images of each working condition are different. Compared with other working

conditions, the image corresponding to normal working conditions is longer. Different slice SDP images are different in mode size and edge shape. For example, the image of rolling fault 1 is more complete, while the image of ball fault 2 is thinner. After graying and binarization, each pixel value of the image is only 0 or 1.

Figure 12: Component signal and mean image of ball fault 1.
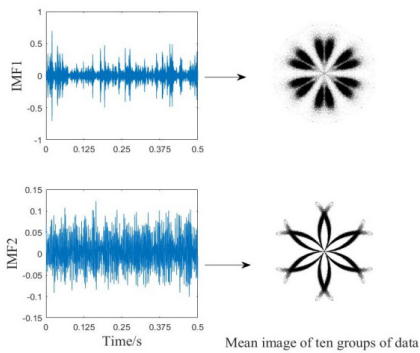
Figure 13: Component signal and mean image of ball fault 2.
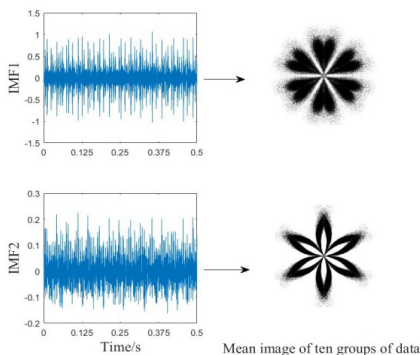
Figure 14: Component signal and mean image of inner ring fault 1.

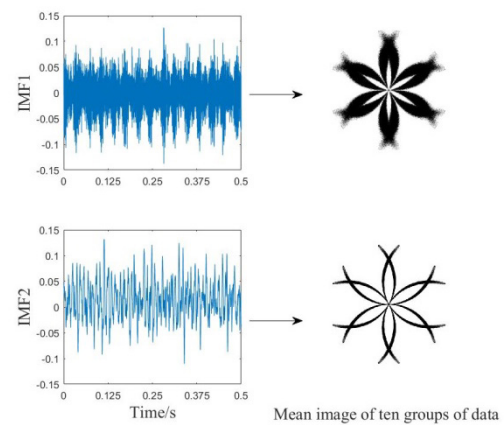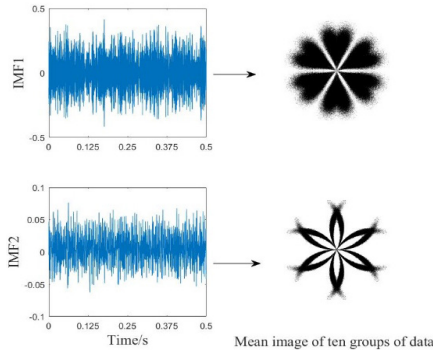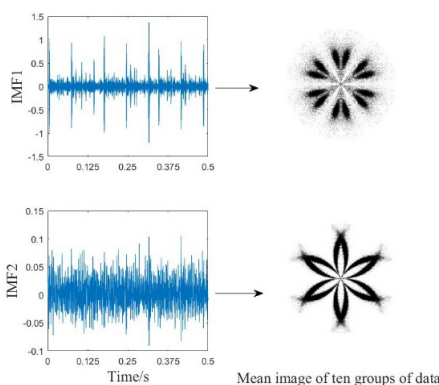**Figure 15:** Component signal and mean image of inner ring fault 2.
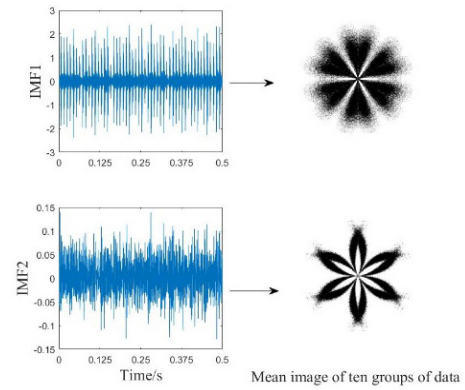
Figure 16: Component signal and mean image of outer ring fault 1.
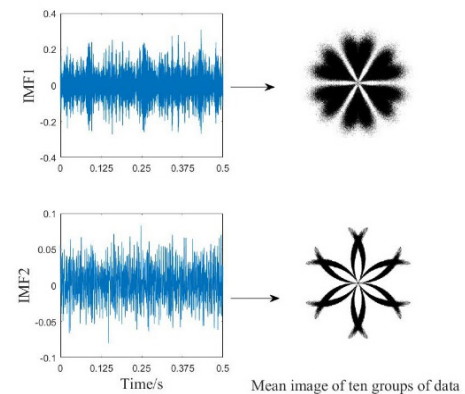
Figure 17: Component signal and mean image of outer ring fault 2.
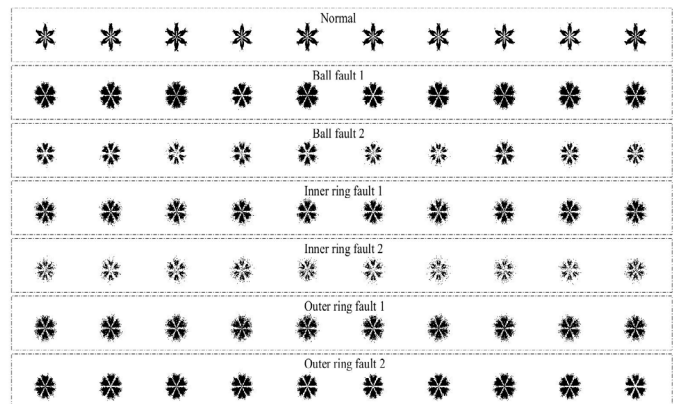
Figure 18: SDP image after binarization.

According to the pixel matrix of ten images, average the pixel values of the corresponding pixels of ten images. This method can get the average image of ten images. As shown in fig.19, each mean value image contains bearing fault information. The features can be extracted from the original ten images and the mean image.

Figure 19: Symmetrized dot pattern's average image.

In order to easily extract fault information and convenient computer calculations, the intercepting SDP image contains 680*680 pixels, so it can be

converted to a matrix of 680*680. After each ten images are averaged, the ten images and the Canberra distance of the mean image, 20 groups are calculated for each working condition, as shown in table 1. According to the data, table 2 can be obtained by

calculating the maximum, minimum and mean values under each condition. As can be seen from the table, bearing failures in different operating conditions have different ranges of Canberra distance. So this Canberra distance is an effective feature of the image.

Table 1: Canberra distance under different working conditions.

Group	Normal	Ball fault 1	Ball fault 2	Inner ring fault 1	Inner ring fault 2	Outer ring fault 1	Outer ring fault 2
1	91.842	127.799	94.346	62.846	50.734	62.779	122.709
2	105.912	125.583	81.593	68.932	45.811	62.862	117.451
3	85.390	126.008	75.930	68.997	43.932	63.418	124.732
4	90.536	128.449	87.020	68.519	52.652	64.011	117.782
5	104.219	127.022	84.667	68.878	43.402	64.453	119.564
6	96.407	126.026	78.030	68.848	47.029	64.389	112.779
7	89.716	126.224	89.371	67.380	47.686	63.108	119.566
8	84.900	125.248	73.769	74.219	56.429	62.843	119.258
9	92.109	127.960	84.252	66.591	54.035	63.531	121.801
10	103.993	128.491	82.875	70.548	44.080	63.819	121.584
11	85.740	128.405	73.315	69.228	44.461	61.777	121.833
12	93.018	128.082	73.161	68.931	39.790	64.701	120.211
13	89.831	128.282	81.242	74.218	49.233	62.704	122.958
14	87.055	126.269	73.198	70.873	54.333	63.408	121.261
15	81.360	126.181	84.621	66.377	47.333	64.131	116.655
16	106.028	127.942	86.272	71.833	49.987	63.211	121.949
17	80.743	121.082	84.119	70.718	41.661	63.739	120.169
18	87.606	126.185	99.512	68.237	45.266	63.977	118.291
19	97.750	127.118	91.386	64.052	56.361	62.648	122.037
20	84.711	124.384	88.488	67.357	48.025	62.612	114.527

Table 2: Maximum, minimum and mean of Canberra distance under different conditions

Group	Normal	Ball fault 1	Ball fault 2	Inner ring fault 1	Inner ring fault 2	Outer ring fault 1	Outer ring fault 2
Maximum value	106.028	128.491	99.512	74.219	56.429	64.701	124.732
Minimum value	80.743	121.082	73.161	62.846	39.790	61.777	112.779
Mean value	91.943	126.637	83.358	68.879	48.112	63.406	119.856

In order to highlight the characteristics of each working condition, the concept of maximum eigenvalue of mean image is introduced. According to eq.11, adding the maximum eigenvalue, the eigenvalue is a very important property of the matrix. At the same time, after a lot of experiments, $\alpha= 0.99$ and $\beta= 0.01$ obtained the best discrimination effect. Table shows the improvement of twenty groups of calculated Canberra distances. Draw the twenty groups of improved Canberra distances into a boxplot

as shown in Figure 20. The upper edge of the blue box in the figure represents the upper quartile of this group of data. The lower edge represents the lower quartile of the data. The red line represents the median of the data. It can be seen from the figure that the improved Canberra distance of each working condition is concentrated in a certain range. And the improved Canberra distance of each working condition fluctuates in different ranges. Therefore, this feature can be used as the basis for fault classification.

Table 3: Improved Canberra distance under different working conditions.

Group	Normal	Ball fault 1	Ball fault 2	Inner ring fault 1	Inner ring fault 2	Outer ring fault 1	Outer ring fault 2
1	599.808	585.610	602.472	616.067	635.017	621.671	587.452
2	591.643	586.422	608.426	613.104	631.214	622.052	589.491
3	600.903	586.327	610.233	613.378	631.417	622.408	586.793
4	599.243	584.689	605.225	614.344	630.062	621.324	590.211
5	592.389	585.871	607.452	613.640	634.565	621.897	589.082
6	597.475	586.243	608.487	612.777	633.479	622.301	591.960

|							
7	599.148	585.626	602.091	614.622	632.753	621.677	588.752
8	601.307	586.674	612.999	611.962	627.054	621.692	589.107
9	598.812	585.515	606.030	616.164	624.711	621.674	587.649
10	593.390	584.476	607.184	613.466	635.512	621.633	588.000
11	601.604	585.041	610.820	613.416	636.399	622.229	587.301
12	597.979	584.992	610.967	612.372	635.816	621.689	588.475
13	599.521	584.949	608.604	612.390	631.697	622.002	587.242
14	600.243	585.982	612.710	613.155	624.871	622.509	587.722
15	602.067	586.248	603.533	614.643	629.261	621.406	589.584
16	591.196	585.485	603.497	612.328	627.941	621.420	587.472
17	601.921	588.744	605.987	611.279	636.410	621.900	588.585
18	599.889	586.275	599.564	615.249	633.736	621.582	589.060
19	595.858	585.423	602.989	615.368	627.484	622.823	587.987
20	600.680	587.235	603.939	615.407	628.799	621.494	590.830
Maximum value	602.067	588.744	612.999	616.164	636.410	622.823	591.960
Minimum value	591.196	584.476	599.564	611.279	624.711	621.324	586.793
Mean value	598.254	585.891	606.660	613.757	631.410	621.869	588.638
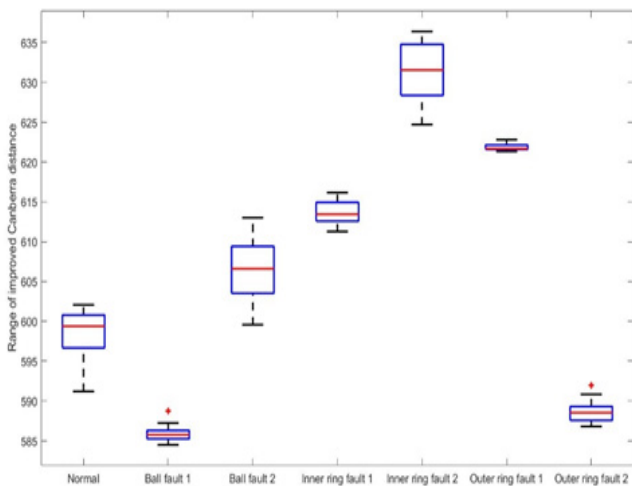
Figure 20: Range of improved Canberra distance under different working conditions.

Finally, we use the improved Canberra distance to diagnose the type of fault. The main algorithm is to set the upper and lower limits of the improved Canberra distance for each condition to determine the type of fault. First you need to calculate the difference between the maximum and minimum distances to improve Canberra for each condition. Select the minimum value of the difference as one of the conditions for calculating the upper and lower bounds. The average of each working condition plus half of the minimum difference is taken as the upper bound. The mean of each condition is subtracted by half of the minimum difference as the lower limit. Judgment range of each condition is shown in Table 4.

Comparative Experiments

The above experiments are based on Case Western Reserve University to analyze the experiments. Here, the validity of the above method is verified using its own platform, and the experimental equipment is shown in fig.21. The speed and horsepower of the motor can be controlled by the speed controller. The speed can be rotated in the range of 0 r/min and 3600 r/min when there is no load, and also the bearings have various failure types to meet the experimental requirements.

Table 4: Comparison of accuracy between original Canberra distance and improved Canberra.

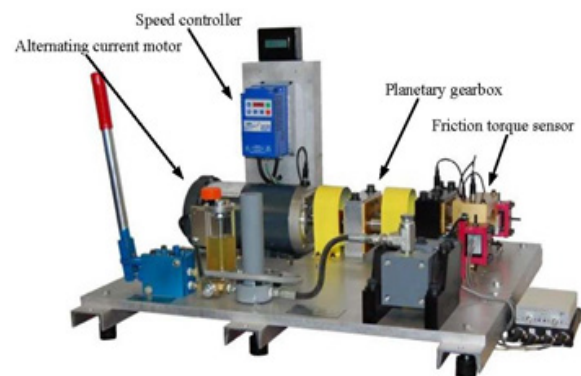| Group	Original Canberra Distance	Present method
1	65.00%	98.00%
2	66.33%	99.67%
3	63.33%	98.67%
4	67.00%	99.00%
5	66.00%	99.33%
6	71.33%	98.00%
7	68.00%	99.33%
8	69.33%	100.00%
9	67.00%	100.00%
10	68.67%	97.67%
Mean value	67.20%	98.97%

Figure 21: Experimental platform.

Comparative Experiment 1: with original Canberra distance

Calculate the improved Canberra distance of a layer of VMD decomposition, and test it randomly. It can be seen from Table

4 that the average accuracy of the improved Canberra distance in judging the type of rolling bearing fault is 98.97%. Then use the same conditions and the same method to calculate the accuracy of original canberra distance. A layer of VMD is used to decompose the data, and the data is divided into 10 groups and converted into 10 SDP images. The converted image is binarized, and the mean image of ten images is obtained. Only the Canberra distance of ten images and the mean image is calculated. Using the mean value of Canberra distance, calculate the range of original canberra distance for each working condition, and then calculate the accuracy of ten groups of original canberra distance as shown in tab.12. The average accuracy of our method is 97.67%. The average accuracy of improved Canberra distance is 31.77% higher than that of original canberra distance.

Comparative Experiment 2: with different decomposition methods

There are other signal decomposition methods similar to those in this paper. EMD, EEMD and CEEMD are selected to decompose the original signal. The purpose of EMD is to decompose the signal into a superposition of intrinsic mode function. After testing, it is found that the first intrinsic mode function of different decomposition methods contains useful information of the signal, so the first intrinsic mode function is selected as the decomposed data. Convert the data into SDP images, calculate the mean image, and then calculate the Canberra distance and the maximum eigenvalues. According to the method in this paper, the corresponding ranges are obtained respectively, and the accuracy is calculated, as shown in tab.5.

Table 5: Accuracy of various decompositions.

Group	EMD	EEMD	CEEMD	Present method
1	89.67%	89.33%	95.67%	98.00%
2	93.67%	92.33%	97.00%	99.67%
3	94.67%	92.33%	96.33%	98.67%
4	91.33%	92.33%	96.00%	99.00%
5	92.67%	89.00%	94.33%	99.33%
6	92.67%	89.67%	97.00%	98.00%
7	93.33%	93.00%	95.67%	99.33%
8	91.00%	94.00%	96.00%	100.00%
9	90.67%	94.67%	93.67%	100.00%
10	88.67%	91.33%	95.67%	97.67%
Mean value	91.83%	91.80%	95.73%	98.97%

The average accuracy of EMD decomposition is 91.83%, the maximum accuracy is 94.67%, and the minimum accuracy is 88.67%. The average accuracy of EEMD decomposition is 91.80%, the maximum accuracy is 97.00%, and the minimum accuracy is 89.00%. The average accuracy of CEEMD decomposition is 95.73%, the maximum accuracy is 97.00%, and the minimum accuracy is 93.67%. Compared with the EMD decomposition method, the accuracy of the method in this paper is increased by 7.14%, 7.17% higher than that of the EEMD decomposition method, and 3.24% higher than that of CEEMD.

Conclusion

In this paper, a method for diagnosing bearings based on VMD decomposition and Canberra distance in SDP images is investigated. The accuracy of the method in this paper is 98.97% in bearing fault diagnosis. In comparative experiment 1, the improved Canberra distance method improves the accuracy. In comparative experiment 2, the present method has better

diagnostic effect than other decomposition methods. In two comparative experiments, the present has high classification performance. In future work, we propose to improve the processing speed of this method. In addition, improving image quality is also a feasible research direction in the future. This method provides a new idea for signal processing. Signal classification based on image features can be applied in other fields.

References

1. Lin, H., Wu, F., & He, G. (2020). Rolling bearing fault diagnosis using impulse feature enhancement and nonconvex regularization. *Mechanical Systems and Signal Processing, 142*, 106790. https://doi.org/10.1016/j.ymssp.2020.106790

2. Zi, W., & Zhu, C. (2020). A new model for analyzing the vibration behaviors of rotor-bearing system. *Communications in Nonlinear Science and Numerical Simulation, 83*, 105130. https://doi.org/10.1016/j.cnsns.2019.105130

3. Wang, H., Liu, Z., Peng, D., & Qin, Y. (2019). Understanding and learning discriminant features based on multiattention 1DCNN for wheelset bearing fault diagnosis. *IEEE Transactions on Industrial Informatics, 16*(9), 5735-5745. https://doi.org/10.1109/TII.2019.2955540

4. Xia, T., Zhuo, P., Xiao, L., Du, S., Wang, D., & Xi, L. (2021). Multi-stage fault diagnosis framework for rolling bearing based on OHF Elman AdaBoost-Bagging algorithm. *Neurocomputing, 433*, 237-251. https://doi.org/10.1016/j.neucom.2020.10.003

5. Wang, T., Liu, Z., Lu, G., & Liu, J. (2020). Temporal-spatio graph based spectrum analysis for bearing fault detection and diagnosis. *IEEE Transactions on Industrial Electronics, 68*(3), 2598-2607. https://doi.org/10.1109/TIE.2020.2975499

6. Liu, D., Cheng, W., & Wen, W. (2021). Intelligent cross-condition fault recognition of rolling bearings based on normalized resampled characteristic power and self-organizing map. *Mechanical Systems and Signal Processing, 153*, 107462. https://doi.org/10.1016/j.ymssp.2020.107462

7. Li, X., Zhang, W., & Ding, Q. (2019). Understanding and improving deep learning-based rolling bearing fault diagnosis with attention mechanism, *Signal processing, 161*, 136-154. https://doi.org/10.1016/j.sigpro.2019.03.019

8. Niu, G., Wang, X., Golda, M., Mastro, S., & Zhang, B. (2021). An optimized adaptive PReLU-DBN for rolling element bearing fault diagnosis. *Neurocomputing, 445*, 26-34. https://doi.org/10.1016/j.neucom.2021.02.078

9. Hoang, D-T., & Kang, H-J. (2019). A survey on deep learning based bearing fault diagnosis. *Neurocomputing, 335*, 327-335. https://doi.org/10.1016/j.neucom.2018.06.078

10. Li, C., Li, S., Zhang, A., He, Q., Liao, Z., & Hu, J. (2021). Meta-learning for few-shot bearing fault diagnosis under complex working conditions. Neurocomputing, 439, 197-211. https://doi.org/10.1016/j.neucom.2021.01.099

11. Guo, S., Zhang, B., Yang, T., Lyu, D., & Gao, W. (2019). Multi-task convolutional neural network with information fusion for bearing fault diagnosis and localization. *IEEE Transactions on Industrial Electronics, 67*(9), 8005-8015. https://doi.org/10.1109/TIE.2019.2942548

12. Zhang, K., Xu, Y., Liao, Z., Song, L., & Chen, P. (2021). A novel Fast Entrogram and its applications in rolling bearing fault diagnosis. *Mechanical Systems and Signal Processing, 154*, 107582. https://doi.org/10.1016/j.ymssp.2020.107582

13. Wang, H., Liu, Z., Peng, D., & Cheng, Z. (2021). Attention-guided joint learning CNN with noise robustness for bearing fault diagnosis and vibration signal denoising. ISA transactions, 128(B), 470-484. https://doi.org/10.1016/j.isatra.2021.11.028

14. Ji, F., & Tay, W. P. (2019). A Hilbert space theory of generalized graph signal processing. *IEEE Transactions on Signal Processing, 67*(24), 6188-6203. https://doi.org/10.1109/TSP.2019.2952055

15. Yang, J., Huang, D., Zhou, D., & Liu, H. (2020). Optimal IMF selection and unknown fault feature extraction for rolling bearings with

different defect modes. Measurement, 157, 107660. https://doi.org/10.1016/j.measurement.2020.107660

16. Cheng, J., Yang, Y., Shao, H., Pan, H, Zheng, J., & Cheng, J. (2022). Enhanced periodic mode decomposition and its application to composite fault diagnosis of rolling bearings. ISA transactions, 125, 474-491. https://doi.org/10.1016/j.isatra.2021.07.014

17. Cheng, J., Yang, Y., Li, X., & Cheng, J. (2021). Adaptive periodic mode decomposition and its application in rolling bearing fault diagnosis. *Mechanical Systems and Signal Processing, 161*, 107943. https://doi.org/10.1016/j.ymssp.2021.107943

18. Haidong, S., Junsheng, C., Hongkai, J., Yu, Y., & Zhantao, W. (2020). Enhanced deep gated recurrent unit and complex wavelet packet energy moment entropy for early fault prognosis of bearing. *Knowledge-Based Systems, 188*, 105022. https://doi.org/10.1016/j.knosys.2019.105022

19. Chen, G., Liu, M, & Chen, J. (2020). Frequency-temporal-logic-based bearing fault diagnosis and fault interpretation using Bayesian optimization with Bayesian neural networks. *Mechanical Systems and Signal Processing, 145*, 106951. https://doi.org/10.1016/j.ymssp.2020.106951

20. Islam, M. M. M., Prosvirin, A. E., & Kim, J-M. (2021). Data-driven prognostic scheme for rolling-element bearings using a new health index and variants of least-square support vector machines. *Mechanical Systems and Signal Processing, 160*, 107853. https://doi.org/10.1016/j.ymssp.2021.107853

21. Albezzawy, M. N., Nassef, M. G., Sawalhi, N. (2020). Rolling element bearing fault identification using a novel three-step adaptive and automated filtration scheme based on Gini index. *ISA transactions, 101*, 453-460. https://doi.org/10.1016/j.isatra.2020.01.019

22. Ding, Y., Jia, M., Miao, Q., & Cao, Y. (2022). A novel time–frequency Transformer based on self–attention mechanism and its application in fault diagnosis of rolling bearings. *Mechanical Systems and Signal Processing, 168*, 108616. https://doi.org/10.48550/arXiv.2104.09079

23. Li, W., Li, B., Yuan, C., Li, Y., Wu, H., Hu, W., & Wang, F. (2020). Anisotropic convolution for image classification. *IEEE Transactions on Image Processing, 29*, 5584-5595. https://doi.org/10.1109/TIP.2020.2985875

24. Park, J., Kim, Y., Na, K., Youn, B. D., Chen, Y., Zuo, M. J., Bae, Y-C. (2022). An image-based feature extraction method for fault diagnosis of variable-speed rotating machinery. *Mechanical Systems and Signal Processing, 167*, 108524. https://doi.org/10.1016/j.ymssp.2021.108524

25. Sun, Y., & Li, S. (2022). Bearing fault diagnosis based on optimal convolution neural network. Measurement, 110702. https://doi.org/10.1016/j.measurement.2022.110702

26. Sun, Y., Xu, B., & Wang, X. (2021). Pseudo fourth-order moment based bearing fault feature reconstruction and diagnosis. *ISA transactions, 118*, 238-246. https://doi.org/10.1016/j.isatra.2021.02.005

27. Sun, Y., Li, S., & Wang, Y., Wang, X. (2021). Fault diagnosis of rolling bearing based on empirical mode decomposition and improved manhattan distance in symmetrized dot pattern image. *Mechanical Systems and Signal Processing, 159*, 107817. https://doi.org/10.1016/j.ymssp.2021.107817

28. Sun, Y., Li, S., & Wang, X. (2021). Bearing fault diagnosis based on EMD and improved Chebyshev distance in SDP image. *Measurement, 176*, 109100. https://doi.org/10.1016/j.measurement.2021.109100